Bulletin of the Seismological Society of America, Vol. 95, No. 5, pp. 1654–1665, October 2005, doi: 10.1785/0120030181

Ⓔ

Inverting for Slip on Three-Dimensional Fault Surfaces Using Angular Dislocations

by Frantz Maerten,* Phillip Resor,† David Pollard, and Laurent Maerten*

Abstract The increasing quality of geodetic data (synthetic aperture radar interferometry [InSAR] dense Global Positioning System [GPS] arrays) now available to geophysicists and geologists are not fully exploited in slip-inversion procedures. Most common methods of inversion use rectangular dislocation segments to model fault ruptures and therefore oversimplify fault geometries. These geometric simplifications can lead to inconsistencies when inverting for slip on earthquake faults, and they preclude a more complete understanding of the role of fault geometry in the earthquake process.

We have developed a new three-dimensional slip-inversion method based on the analytical solution for an angular dislocation in a linear-elastic, homogeneous, isotropic, half-space. The approach uses the boundary element code Poly3D that employs a set of planar triangular elements of constant displacement discontinuity to model fault surfaces. The use of triangulated surfaces as discontinuities permits one to construct fault models that better approximate curved three-dimensional surfaces bounded by curved tiplines: shapes that commonly are imaged by three-dimensional reflection seismic data and inferred from relocated aftershock data.

We demonstrate the method's ability to model three-dimensional rupture geometries by inverting for slip associated with the 1999 Hector Mine earthquake. The resulting model avoids displacement anomalies associated with the overlapping rectangular dislocations used in previous models, improving the fit to the geodetic data by 32%, and honors the observed surface ruptures, thereby allowing more direct comparisons between geologic and geodetic data on slip distributions.

Online Material: Hector Mine input files and file format description.

Introduction

Geodetic inversions are a useful tool for estimating kinematic source parameters of earthquakes (e.g., Stein and Barrientos, 1985; Lin and Stein, 1989; Freymueller *et al.*, 1994; Feigl *et al.*, 1995; Yu and Segall, 1996; Wright *et al.*, 1999; Reilinger *et al.*, 2000). Using static surface displacements associated with a given earthquake researchers seek to better understand earthquake rupture processes by inverting for fault geometry and/or slip distributions. The challenge is to find the most accurate geometry and slip distribution supported by the data. The increasing availability of spatially rich geodetic data, specifically dense Global Positioning System (GPS) networks and synthetic aperture radar interferometry (InSAR), offers researchers opportunities to construct increasingly complex geometric and kinematic models of earthquake ruptures (e.g., Johnson *et al.*, 2001; Bürgmann *et al.*, 2002; Jónsson *et al.*, 2002; Sandwell *et al.*, 2002; Simons *et al.*, 2002). Inverting for both fault geometry and slip is a challenging nonlinear problem. Here we prescribe a realistic geometry and carry out the linear inversion for slip. We show, in particular, how spatially dense data in the near-field admit models that incorporate realistic geometry when estimating coseismic slip.

Geological and geophysical observations reveal that faults typically are not single planar surfaces bounded by rectangular tiplines but are composed of individual curved surfaces with curved tiplines organized as multiple echelon,

*Present address: IGEOSS, Cap Omega, Rond Point Benjamin Franklin, CS3951, 34960 Montpellier Cedex 2, France.

†Present address: Department of Earth and Environmental Sciences, Wesleyan University, Middletown, Connecticut 06459.

conjugate, and intersecting segments. This conceptual model of fault geometry is based on observations from a variety of sources including studies of earthquake surface ruptures (e.g., Zhang *et al.*, 1999; Lin *et al.*, 2001; Aydin and Kalafat, 2002; Treiman *et al.*, 2002), exhumed faults (e.g., Martel, 1990; Cartwright *et al.*, 1995; Willemse *et al.*, 1997; Peacock, 2002), reflection seismology (e.g., Willemse et al., 1996; Walsh *et al.*, 1999; Maerten et al., 2000; Kattenhorn and Pollard, 2001), and aftershock patterns (e.g., Waldhauser and Ellsworth, 2000; Carena and Suppe, 2002; Kilb and Rubin, 2002; Chiaraluce *et al.*, 2003). To more precisely estimate coseismic slip and thus to advance the understanding of earthquake source parameters we advocate the incorporation of curved fault surfaces and tiplines in geodetic inversions of coseismic deformation. Previous workers have attempted to incorporate nonplanar geometry by constructing faults from multiple rectangular dislocations after the solution of Okada (1985) (e.g., Johnson *et al.*, 2001; Jónsson *et al.*, 2002; Simons *et al.*, 2002). Although these models have proved effective in certain applications, the curved surfaces and tiplines of faults cannot be modeled with a set of rectangular dislocation segments without introducing nonphysical gaps and overlaps.

In this article we present a new method for slip inversion based on the solution for an angular dislocation in an elastic half-space, employing triangular elements of constant displacement discontinuity to model fault surfaces. Discretization of surfaces into triangular elements allows for the construction of three-dimensional fault surfaces that more closely approximate curviplanar surfaces and curved tiplines without introducing overlaps or gaps, consistent with the full extent of available data. We demonstrate the strengths of this new method through a brief analysis of the fault rupture due to the 1999 Hector Mine earthquake (M_w 7.1). We start with a planar segmented fault model based on the work of Jónsson *et al.* (2002) and compare these results to models that more closely honor the observed surface rupture pattern along multiple curved and intersecting fault segments. The resulting inversions show that models that more closely honor the geometry of the surface ruptures also yield significant improvements in the fit to the geodetic data.

Method

Displacements $\mathbf{d}^p$ at points (p) on the Earth's surface due to slip $\mathbf{m}^e$ on elements (e) of a buried fault can be described by a set of linear equations

$$\mathbf{d}^p = \mathbf{G}^{e,p}\mathbf{m}^e + E, \tag{1}$$

where E are the observational errors and $\mathbf{G}^{e,p}$ are the influence coefficients, or Green's functions, that describe how slip on a fault element produces displacement at the Earth's surface. This set of equations can be used to forward model surface displacements from a known fault geometry and slip distribution, or as an inverse problem to model subsurface fault geometry and slip from an observed set of surface displacements. Inversion for fault geometry is highly nonlinear and thus computationally intensive even for very simple geometries (Cervelli *et al.*, 2001), while inversion for slip is a linear inverse problem and thus relatively straightforward. In this article we present a new approach to solving the linear inverse problem, inverting for slip on faults with geometry that is determined *a priori.* Ideally the geometry is constrained through integration of multiple data sets such as mapped surface ruptures, high-precision aftershock locations, reflection seismology, and/or the results of nonlinear inversion for a simplified fault geometry (e.g., for the Hector Mine earthquake, see Hurst *et al.*, 2000; Jónsson *et al.*, 2002; Simons *et al.*, 2002).

To implement the inverse problem, we seek a solution that simultaneously minimizes the L-2 norm (hereafter annotated with $\| \|_2$) of the data misfit and of the model roughness. This approach allows fitting of the data to a desired threshold while introducing the geologic concept that slip distributions are relatively smooth rather than oscillatory (Harris and Segall, 1987). Minimizing the model roughness acts to prevent overfitting of noisy data and compensates for underdetermined model parameters and geometric inaccuracies. The slip inversion problem can thus be written as

$$\min\left[\|\mathbf{Gm} - \mathbf{d}\|_2 + \varepsilon^2\|\mathbf{Dm}\|_2\right], \tag{2}$$

where the first term $\|\mathbf{Gm}\text{-}\mathbf{d}\|_2$ is the L-2 norm of the data misfit and the second term $\varepsilon^{-2}\|\mathbf{Dm}\|_2$ is a measure of the model roughness. The data misfit is calculated by subtracting the observed displacements $\mathbf{d}$ from the predicted displacements, which are themselves calculated by multiplying the Green's functions $\mathbf{G}$ by the modeled slip $\mathbf{m}$. In the case of InSAR data, the model also includes apparent surface displacements that appear as a uniform tilting associated with errors in modeling orbital parameters during data processing (Hanssen, 2001). The model roughness term $\varepsilon^{-2}\|\mathbf{Dm}\|_2$ is composed of a scalar smoothing parameter ε multiplied by the L-2 norm of a discrete second-order difference operator $\mathbf{D}$. Inclusion of this term acts to minimize the second derivative, or Laplacian of the modeled slip $\nabla^2\mathbf{m}$, and thus minimizes the nondimensional model roughness, defined as the change in fault slip per length of fault squared and typically reported in units of cm/km^2 (Harris and Segall, 1987). The value of ε controls the amount of smoothing and may be determined either from a tradeoff curve, seeking to balance smoothing with data fitting or by cross validation (Harris and Segall, 1987, Du *et al.*, 1992).

The approach we take to solve the slip inversion problem differs from previous work in the form of the Green's functions and the smoothing operator $\mathbf{D}$. The Green's functions we use are based on the analytical solution for the elastic boundary value problem of an angular dislocation (Fig. 1a) in an infinite whole- or semi-infinite half-space composed of a homogeneous and isotropic linear-elastic material (Comninou and Dundurs, 1975). Comninou and Dun-

durs (1975) extended the solution for an angular dislocation in a whole-space (Yoffe, 1960) to an elastic half-space. In the half-space solution an angular dislocation lies in a vertical plane with one leg parallel to the z axis and a second leg inclined at angle β from the first. A dislocation segment can be constructed by superimposing two coplanar angular dislocations with opposite Burger's (slip) vectors and equal angles β, at two different vertex locations, ξ_1 and ξ_2 (Fig. 1b). The two dislocations cancel each other except for the area of underlap, the dislocation segment. The solution for a triangular dislocation patch (Fig. 1c) is generated by superposition of three angular dislocation segments that share a common set of vertices, ξ_1 through ξ_3 (Jeyakumaran *et al.*, 1992). The vertical legs of the dislocations cancel leaving only the triangular dislocation patch. Fault surfaces can be constructed by joining multiple triangular patches or elements. This solution was implemented in a C-language computer program, Poly3D (Thomas, 1993), that calculates the three-dimensional components of displacement, strain, and stress anywhere in the elastic body. The first author has subsequently rewritten the code in C++ to (1) make the code modular, thereby facilitating the development of new applications such as the inverse formulation; (2) correct the displacement field for points located underneath dislocation elements; (3) optimize the computation time; and (4) develop a three-dimensional graphical user interface (GUI) for the creation of Poly3D models and visualization of model results. The Poly3D code provides a direct kinematic solution with prescribed displacement discontinuities on the elements making up the model faults, and a mechanical solution that prescribes a uniform remote stress or strain state and tractions at the midpoint of each element, or mixed boundary conditions. For slip inversion we use the kinematic solution for the Green's functions implemented in the code Poly3Dinv, Compiled codes and documentation are available at http://pangea.stanford.edu/research/geomech/Software/Software.htm.

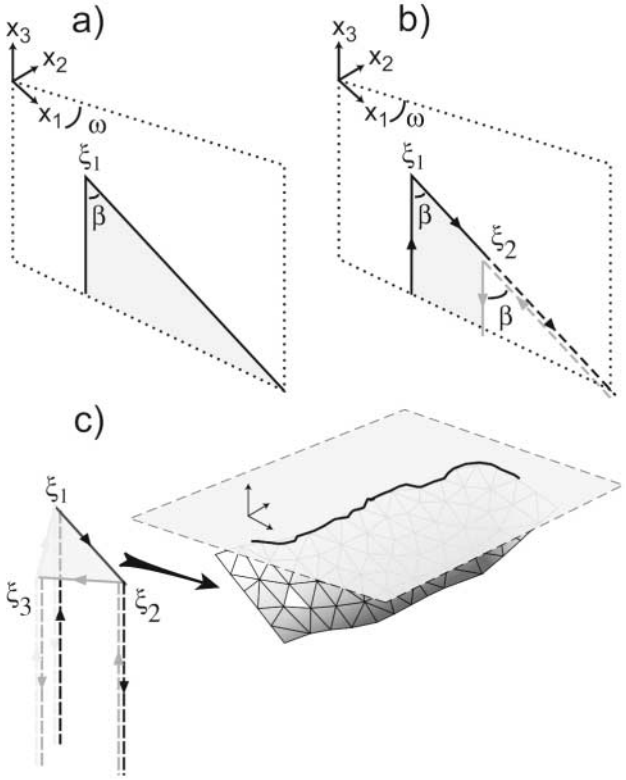

Figure 1. Construction of a triangular dislocation patch from a set of six angular dislocations. (a) A single vertical angular dislocation located at point ξ_1 in a homogeneous elastic half-space where Cartesian coordinate x_3 is vertical, positive upward, and the x_1–x_2 plane is the traction-free surface. β is the angle between the vertical and sloping legs of the dislocation, and ω is the smaller angle between the x_1 axis and the strike line of the dislocation plane. (b) Two coplanar angular dislocations of equal angles β may be superimposed to create a dislocation segment with vertical legs. (c) A triangular dislocation patch can be generated by superimposing three dislocation segments that share three common locations (ξ_1, ξ_2, ξ_3). The vertical dislocation lines cancel leaving a tilted triangular dislocation element (after Thomas, 1993).

Due to the use of traingular elements, our calculation of the discrete Laplacian operator ∇^2 also differs from previous slip inversions. Instead of a finite-difference formulation we use the scale-dependent umbrella operator (Desbrun *et al.*, 1999),

$$\nabla^2 m_i = \frac{2}{L_i} \sum_{j=1}^{3} \frac{m_j - m_i}{h_{ij}}, \tag{3}$$

to approximate the discrete Laplacian for a triangulated two-manifold. For a triangular element i (Fig. 2), with adjacent elements j on its three sides ($j = 1{:}3$), h_{ij} represents the distance from the center of element i to the center of element j, m_j is the slip vector of element j, and L_i is the sum of the

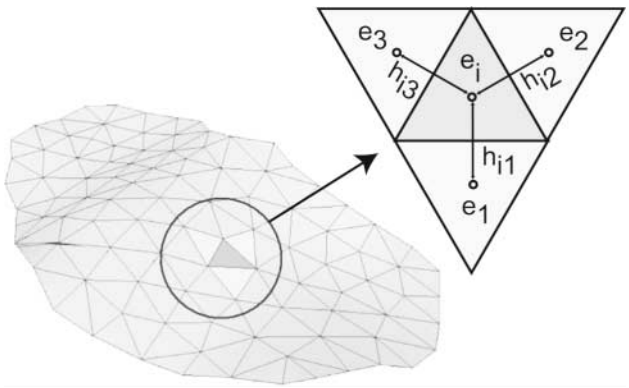

Figure 2. Discrete Laplacian operator used in Poly3Dinv to smooth the slip distribution. Each displacement discontinuity component of an element (e_i, dark gray) is smoothed relative to its adjoining neighbors (e_j, light gray). Distances between e_i and e_j centers are h_{ij}.

element center distances, $L_i = \sum_{j=1}^{n} h_{ij}$. Rearranging to isolate diagonal (m_i) and off-diagonal terms (m_j) yields a smoothing operator of the form

$$m_j\left(\frac{2}{Lh_{ij}}\right) + m_i\left(-\frac{2}{L}\sum\frac{1}{h_{ij}}\right). \quad (4)$$

Superimposing this relation for all elements of the model yields a smoothing operator (sparse matrix) that is used within the least-squares formulation to minimize the roughness of the solution. This operator is dependent on the length scale of the model, an effect that can be removed by normalizing by the average value of h_{ij}.

In order to solve the linear minimization problem (equation 2) , we use a weighted damped least-squares approach:

$$\mathbf{m} = (\mathbf{G}^{\mathrm{T}}\,\mathbf{W}_{\mathrm{e}}\mathbf{G} + \varepsilon^2\mathbf{D}^{\mathrm{T}}\mathbf{D})^{-1}\mathbf{G}^{\mathrm{T}}\mathbf{W}_{\mathrm{e}}\mathbf{d}, \quad (5)$$

where $\mathbf{W}_{\mathrm{e}}$ is a weighting matrix that defines the relative contribution of each data point to the total prediction error (Menke, 1989). $\mathbf{W}_{\mathrm{e}}$ is typically a diagonal matrix calculated from the normalized inverse of the data measurement errors. In multiple inversions entire data sets may also be weighted relative to one another based on the relative measurement precision of each data set (e.g., InSAR vs. GPS) (Jónsson *et al.* 2002). Equation (4) is solved given the fault geometry and the input data (GPS or InSAR).

Additional constraints can be applied to reach a solution that is consistent with geological concepts of faults. For example, a zero slip constraint may be applied at known fault tips. These may include the base of the seimogenic crust and lateral fault tiplines extending downward from mapped rupture terminations at the earth's surface. In addition, individual slip components can be constrained to be unidirectional, for example, right lateral, left lateral, reverse or normal only, or any combination of dip slip and strike slip. These constraints are imposed by using an iterative solution algorithm derived from the fast nonnegative least squares (FNNLS) solver (Bro and de Jong, 1997) to solve equation (4) with any combination of nonnegative, nonpositive, or unconstrained slip components.

Application to the 1999 Hector Mine Earthquake

We have chosen to evaluate the new approach to slip inversion using the 16 October 1999 Hector mine earthquake (M_{w} 7.1) because of the complexity of the observed surface rupture geometry (Fig. 3) and the availability of high-quality data (Fig. 4) (e.g., Jónsson *et al.*, 2002; Sandwell *et al.*, 2002; Simons *et al.*, 2002; Treiman *et al.*, 2002). The Harvard CMT fault-plane solution for the event (Dziewonski *et al.*, 2000) has a moment of 5.98×10^{19} N m, a strike of 336°, and dip of 80° for the inferred primary nodal plane, and a rake of 174° for slip on this plane (Table 1).

The Hector Mine Earthquake ruptured a set of fault segments with a trace length of ~48 km in the Mojave Desert of California (Treiman *et al.*, 2002). Surface ruptures occurred on portions of the Lavic Lake fault, an unnamed northeast branch fault, and two strands of the Bullion fault (Fig. 3). These included intersecting, echelon, and curving fault segments as well as several parallel segments at the southern terminus of the surface rupture. Observed offsets of surface features had a consistent right-lateral sense with a maximum value of 5.25 ± 0.85 m. The sense of vertical offsets was more variable, except in the Bullion Mountains area where there was consistent east-up offset (Treiman *et al.*, 2002).

Moment tensor solutions (e.g, Harvard CMT; Dziewonski *et al.*, 2000), geodetic inversions (Hurst *et al.*, 2000; Jónsson *et al.*, 2002; Simons *et al.*, 2002), and aftershock distributions (Hauksson *et al.*, 2002) all suggest that the faults dip steeply (~72–84°) to the northeast. Multiple geophysical data sets are available for modeling the coseismic rupture associated with the Hector Mine earthquake including broadband seismology, continuous and campaign GPS (Hurst *et al.*, 2000; Agnew *et al.*, 2002) and ascending and descending radar interferograms (InSAR) (Jónsson *et al.*, 2002; Sandwell *et al.*, 2002; Simons *et al.*, 2002). In particular, the availability of highly coherent ascending and descending interferograms permits detailed modeling of near-field deformation (Fialko *et al.*, 2001; Sandwell *et al.*, 2002). Our goals are primarily to evaluate slip inversions using the new method and to demonstrate how using a model that admits more realistic fault geometry may improve fault slip estimates.

A number of previous studies of the Hector Mine earthquake have inverted for coseismic source parameters incorporating geodetic data. The results of these studies are summarized in Table 1. Hurst *et al.* (2000) inverted for a single dislocation source within two weeks of the event using data from the continuously recording Southern California Integrated GPS Network (SCIGN). They solved a nonlinear inversion problem for eight source parameters (x position, y position, length, width, strike, dip, strike slip, dip slip) using a simulated annealing approach. Ji *et al.* (2002) and Kaverina *et al.* (2002) performed joint inversions of geodetic and seismological data for variable fault slip on simplified dipping three-fault models made up of multiple point sources. Sandwell *et al.* (2002) and Price and Bürgmann (2002) created models that more closely honored the geometry of the observed surface trace but with vertical faults. This approach allowed for construction of faults comprised of multiple rectangular segments including along strike heterogeneities without generating gaps or overlaps, but these models are inconsistent with the previously cited evidence for eastward-dipping fault planes. Simons *et al.* (2002) and Jónsson *et al.* (2002) performed inversions using GPS and InSAR data that allowed for more realistic dipping multisegment models. These groups both performed nonlinear inversions for geometry and linear inversion for variable slip

Table 1
Estimates of Source Parameters for the 1999 Hector Mine Earthquake

Model Geometry	Data	Method	Moment (N m)	Primary Nodal Plane			Authors
				Strike	Dip	Rake	
Point	Teleseismic	CMT	5.98×10^{19}	336	80	174	Harvard CMT
Single rectangular dislocation	Continuous GPS	Nonlinear inversion	3.8×10^{19}	330	84.2	154	Hurst *et al.* (2000)
Point sources—3 dipping planes	Strong motion, teleseismic, GPS, surface offsets	Nonlinear wavelet inversion	6.28×10^{19}	—	—	175	Ji *et al.* (2002)
Point sources—3 dipping planes	Broadband, GPS, InSAR	Joint linear inversion	6.8×10^{19}	—	77	180	Kaverina *et al.* (2002)
Regular discretization of vertical fault honoring trace of surface rupture	GPS, InSAR	Linear slip inversion	5.6×10^{19}	—	90	180	Price and Bürgmann (2002)
Rectangular discretization of 5 variably dipping planes	GPS, InSAR	Nonlinear inversion	6.7×10^{19}	—	75–85	—	Simons *et al.* (2002) (Homogeneous half-space model)
Rectangular discretization of 9 dipping planes	GPS, InSAR	Nonlinear inversion	5.93×10^{19}	—	83	175	Jónsson *et al.* (2002)
Triangular discretization of 9 dipping planes	GPS, InSAR	Linear slip inversion	5.44×10^{19}	333	83	175	Model a, this article
Triangular discretization of 2 dipping, irregular fault surfaces	GPS, InSAR	Linear slip inversion	5.39×10^{19}	332	82	175	Model b, this article
Triangular discretization of 6 dipping, irregular fault surfaces honoring trace of surface rupture	GPS, InSAR	Linear slip inversion	5.13×10^{19}	333	83	176	Model c, this article

on their fault segments. The resulting fault models included dipping segments with heterogeneities but also generated gaps and overlaps in the fault surface.

Modeling

We have created a series of fault models to compare the results of our method to published results using rectangular dislocations and to illustrate the ability of this method to incorporate more realistic three-dimensional fault geometries that more closely honor observations of surface rupture geometry and fault dip. The faults in all of the models dip 83° to the east based on the results of nonlinear inversions of geodetic data by Jónsson *et al.* (2002). The faults in each of the models have been discretized into meshes of triangular elements of approximately constant size and equilateral geometry. The total number of elements (~700) was kept nearly constant between models to maintain roughly the same number of degrees of freedom and thus permit direct statistical comparison.

We take as our starting point the geometric model of Jónsson *et al.* (2002) that is comprised of nine planar segments approximating the trace of the Lavic Lake unnamed northeast segment and Bullion faults (Fig. 5a). The panels have been discretized into 783 triangular elements. The large planar panels model the fault geometry at approximately a 6-km scale and have gaps or overlaps at segment boundaries where the strike of the fault changes. The second model incorporates a curviplanar fault surface that approximates the mapped surface ruptures for the Lavic Lake and West Bullion faults and the distribution of aftershocks for the unnamed northeast fault (Fig. 5b). The curviplanar fault surfaces have been discretized into 683 triangular elements. The mapped fault traces have along-strike undulations that are matched by the model fault to the extent possible given the 2.3-km average element size. The minimum radius of curvature that can be modeled by a continuous mesh of equilateral elements of this size is approximately 1.6 km. This figure is based on the radius of curvature of an open tetrahedron formed by three adjoining elements. A third model was constructed to illustrate the strength of this new method in modeling three-dimensional fault surfaces. This model honors the details of the observed surface ruptures at a ~2-km-scale (Fig. 5c) including all six fault segments with observed surface displacements and extends these segments to the northwest and southeast beyond the observed rupture to allow for the possibility of unobserved slip at the surface and/or subsurface slip that extended beyond the mapped surface rupture (see Simons *et al.*, 2002 for further discussion). The model is discretized into 612 triangular elements. The average element side is ~2.6 km resulting in a maximum radius of curvature of ~ 1.8 km.

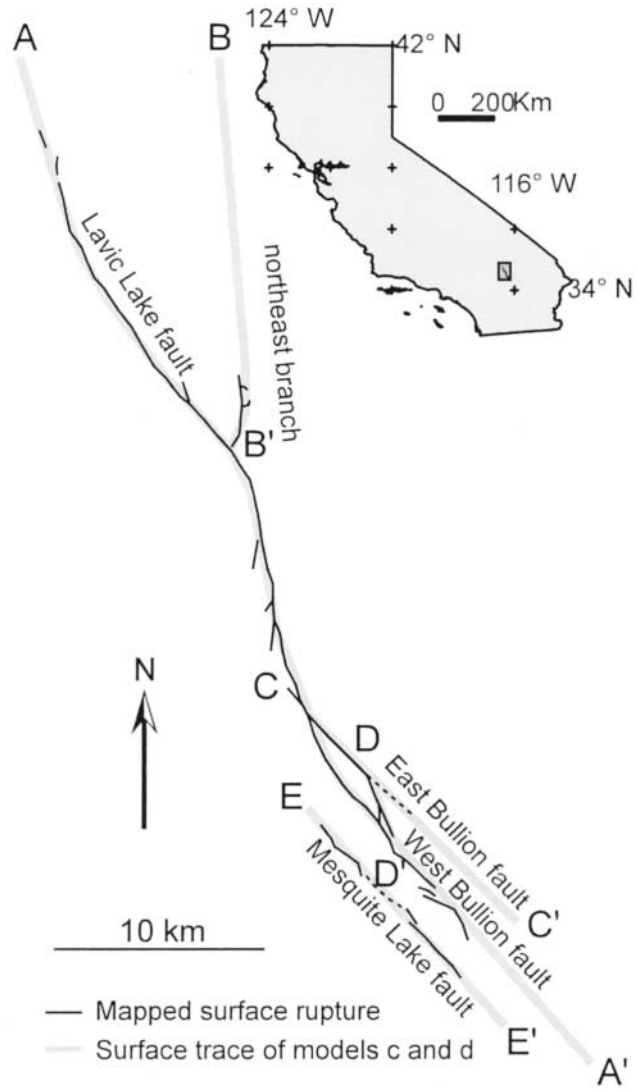

Figure 3. Map of the Hector Mine earthquake surface rupture (black) (Treiman *et al.*, 2002). Gray lines are surface trace of six-segment model (Fig. 5c). Lettered sections refer to graphed segments in Figure 6. Upper right inset shows location of Hector Mine earthquake (dark gray rectangle) in southeastern California.

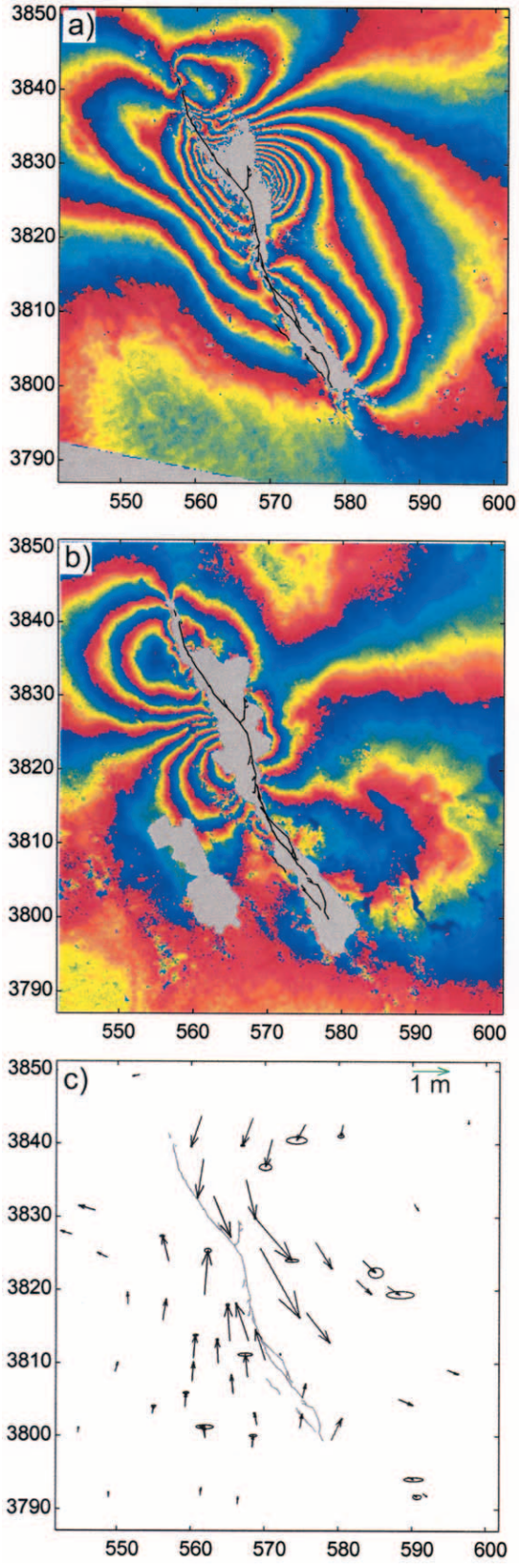

Figure 4. Geodetic data used for slip inversions. Coordinates are northing and easting for UTM zone 11. (a) Descending interferogram of Hector Mine earthquake coseismic deformation (Jónsson *et al.*, 2002) calculated from ERS-2 satellite descending passes on 15 September 1999 and 20 October 1999. (b) Ascending interferogram (Jónsson *et al.*, 2002) calculated from ERS-2 satellite descending passes on 12 November 1995 and 21 November 1999. For parts (a) and (b) each color cycle represents 10 cm of displacement in the satellite line-of-site. The color gradient from red to yellow to blue is in the positive direction, toward the satellite. (c) GPS displacement vectors from Agnew *et al.* (2002). Ellipses represent 2-sigma uncertainty. Scale shown in green in the upper right corner.

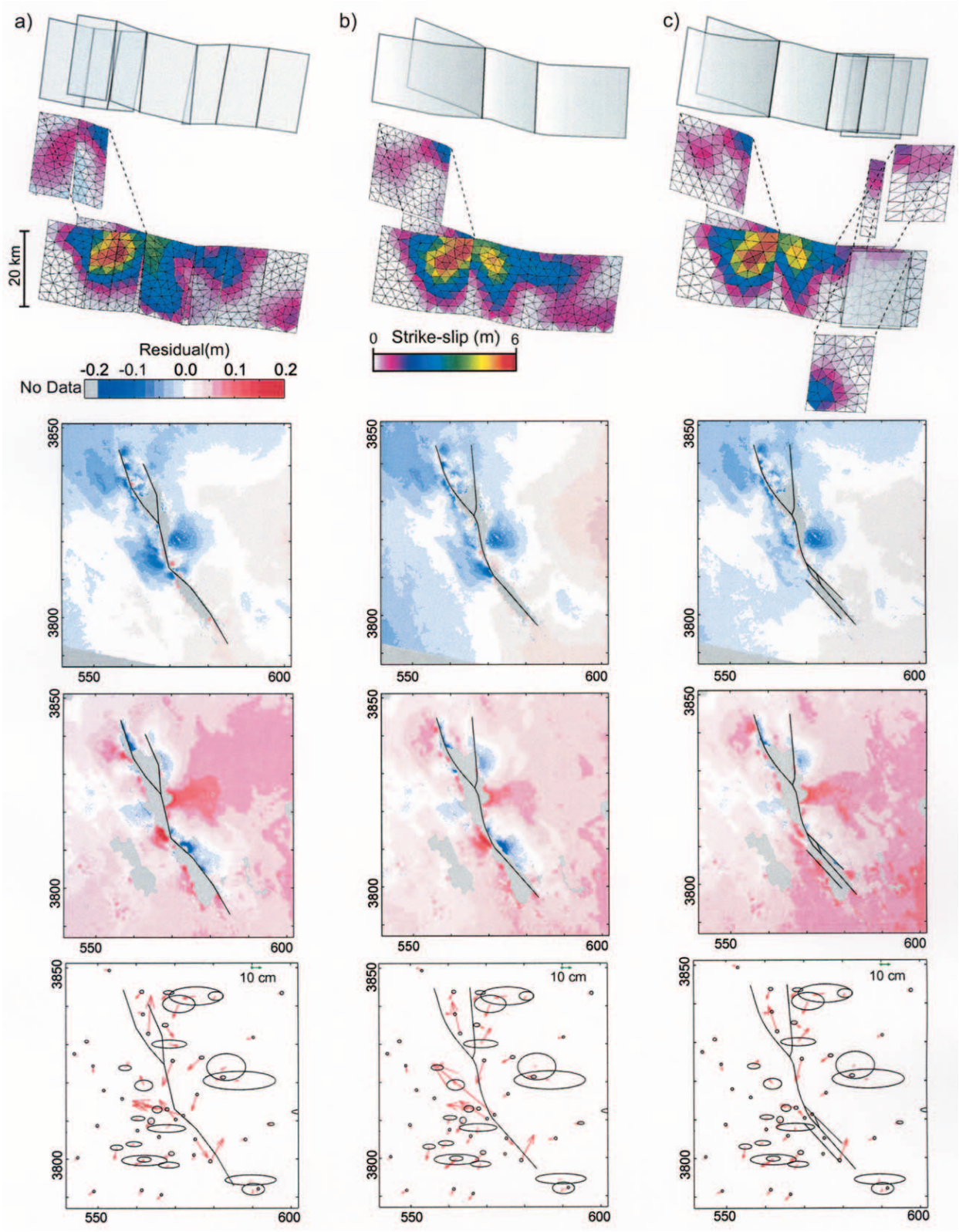

Figure 5. Comparison of fault models including modeled slip distributions and residuals for descending and ascending phase InSAR and GPS data (from top to bottom). (a) Planar segment model after Jónsson *et al.* (2002). (b) Curviplanar model approximating trace of major faults. (c) Six segment model that more closely honors the geometry of the mapped surface ruptures (Fig. 3). Note scale change for GPS residuals in comparison to Figure 4. Coordinates are northing and easting for UTM zone 11. Ⓔ All of the model files are available in the electronic edition of BSSA.

For each geometric model we performed a joint inversion for slip using the decimated ascending and descending InSAR data sets of Jónsson *et al.* (2002) and campaign GPS data (Agnew *et al.*, 2002; Fig. 4). The SAR interferograms are treated as having a constant angle of incidence across the entire image with look vectors of [−0.38, 0.07, −0.92] and [0.38, 0.08, −0.92] for the descending and ascending phase data, respectively. Slip is constrained to be a combination of right-lateral strike slip and east-up dip slip based on the results of previous geodetic (Hurst *et al.*, 2000; Agnew *et al.*, 2002; Jónsson *et al.*, 2002; Sandwell *et al.*, 2002), geologic (Treiman *et al.*, 2002), and seismological investigations (Harvard CMT), (Dziewonski *et al.*, 2000; Ji *et al.*, 2002). Individual data sets (GPS and InSAR) are weighted relative to data uncertainty as outlined by Jónsson (2002). We select the smoothing parameter using a tradeoff curve where we seek the smoothing value that minimizes slip roughness (reported as the mean squared Laplacian of the slip distribution) without significantly increasing data misfit. The value $\varepsilon = 0.07$ yields an average roughness of $\sim 1.7 \times 10^{-8}$ 1/km^2 for model 1 (Fig. 5a) versus 5.7×10^{-7} 1/km^2 for the unsmoothed solution while only reducing the model misfit (weighted residual sum of squares [WRSS]) by 22%. (Ⓔ All of the fault models as well as the data and parameters used for the slip inversions are available in the electronic edition of BSSA.)

Results

The resolved slip patterns in each of our models (Fig. 5) are grossly similar to the results of Jónsson *et al.* (their figure 8a), although we have chosen a slightly rougher solution as our optimal model. For all three fault models the maximum strike-slip is located on the Lavic Lake fault just northwest of the intersection with the northeast branch at approximately 7-km depth. The magnitude of slip is 6.5 m, 6.6 m, and 7.0 m for models a, b, and c, respectively. The dip-slip maximum is also located along the Lavic Lake fault for all three models at approximately 5.5-km depth but moves from north of the intersection with the northeast branch fault in the planar fault model to south of the intersection for the curviplanar fault models. The magnitude of the maximum dip-slip is 2.6 m for models a and b and 3.4 m for model c.

The introduction of parallel segments in the multisegment model leads to slip partitioning between the multiple faults segments in a manner similar to geological observations. Slip on the lavic lake fault decreases to the southeast toward its intersection with the West and East Bullion faults where slip is then partitioned onto each of these parallel segments. The East Bullion fault has a maximum of 1.4 m of slip at its intersection with the Lavic Lake fault and this tapers off to zero slip over about 10 km. The majority of slip, 2.5 m, occurs on the West Bullion fault and continues about 20 km to the south. The Mesquite Lake fault has 3.5 m of slip at ~18-km depth. Slip at this depth is relatively poorly resolved (Bos and Spakman, 2003) and these results are therfore not well constrained.

The seismic moment, moment magnitude, and best-fit double couple (Jost and Herrman, 1989) for each of the models are presented in Table 1. All three models yield a moment magnitude of 7.1 with decreasing total seismic moments. These results are similar but slightly lower than previous estimates of the moment using geodetic and seismic methods. The best double couple for the three models is also similar to previous estimates with primary nodal planes striking 332–333°, dipping 82–83°, and rakes of 175–176°.

The series of models we have constructed fits the observed surface ruptures progressively better; however, we also wish to know if it yields an improved fit to the geodetic data. Goodness of fit is commonly estimated using chi-squared tests that normalize the model residual (WRSS) by the model degree of freedom. This second parameter, however, is difficult to estimate due to correlations between model parameters introduced by smoothing (Cervelli *et al.*, 2001; Jónsson *et al.*, 2002). We argue that by maintaining approximately the same number of elements and the same smoothing parameter, the number of model parameters remains roughly constant and therefore comparison of the WRSS between models is a reasonable estimate of the relative quality of their fit. We therefore compare our models by presenting the change in the WRSS for the combined and individual data sets as well as presenting a graphical representation of model residuals for the three geodetic data sets (Fig. 5).

By incorporating a single curviplanar surface (Fig. 5b) we obtained a 8% improvement in WRSS for the combined data sets in comparison to the planar segment model (Fig. 5a). This model reduces the WRSS for the descending phase InSAR by 14% and the ascending phase InSAR by 22%, however it leads to a 34% increase in WRSS for the GPS data. The image of the descending phase residuals shows a clear reduction in the near-field residuals that is most obvious near the kink between the Lavic Lake and Bullion faults in the original model (Fig. 5a). The kink in the planar segment model creates an area of overlapping fault segments that generates a model residual greater than 10 cm, also observable in the model of Jónsson *et al.* (their figure 9b). In the curviplanar model the residuals in this area are less than 10 cm. Simply smoothing the initial planar-segment model, removing the overlaps and gaps removes this effect and leads to a 2% reduction in the WRSS (results not presented). The increase in the WRSS for the GPS data is largely due to a poorer fit at stations near the northeast branch fault and along the Bullion faults near their intersection with the Lavic Lake fault.

By incorporating all of the segments where surface rupture was observed (Fig. 5c) we obtain a 32% reduction in the total WRSS with a 23% reduction for the descending phase InSAR data, a 45% reduction for the ascending phase InSAR data, and a 57% reduction for the GPS data. This model is our preferred model as it significantly improves the fit to the observed surface ruptures and the geodetic data. The reduction in misfit for the descending phase InSAR data is most noticeable to the northwest of the intersection of the

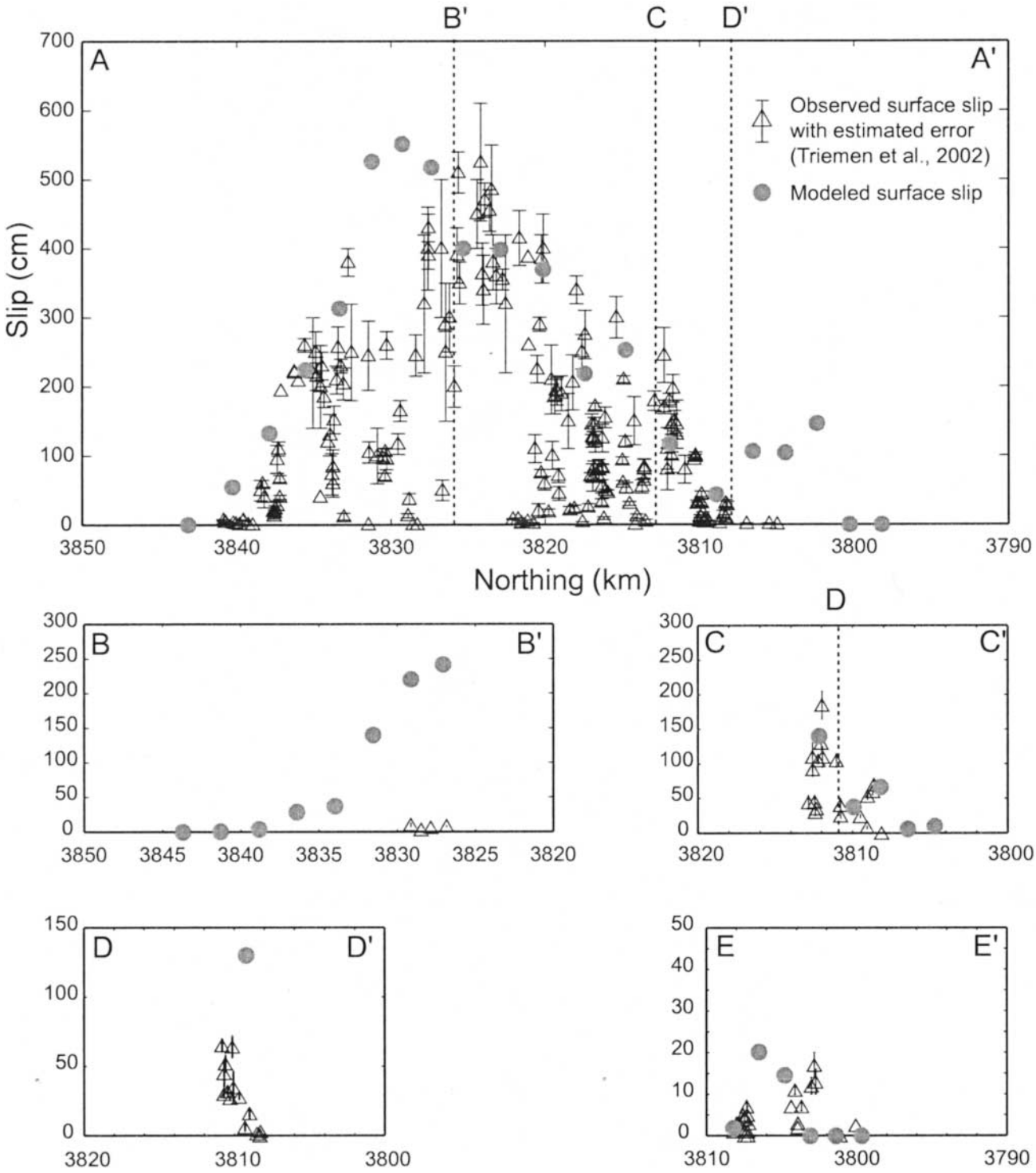

Figure 6. Comparison between the slip of elements at the surface for multisegment fault model (Fig. 5c) and the measured surface slip distribution from Treiman *et al.* (2002). Fault segments are illustrated in Figure 3. AA′, Lavic Lake–West Bullion faults; BB′, northeast branch of the Lavic Lake fault; CC′, East Bullion fault; DD′, linking structure between East and West Bullion faults; EE′, Mesquite Lake fault. Note different ordinate scales for DD′ and EE′. Fault intersections are marked with dashed lines.

Bullion and Lavic lake faults where the previous models had residuals greater than 10 cm, which are reduced to less than 5 cm. The high residuals in the ascending InSAR and GPS data near the intersection of these faults are also reduced.

The results of the multisegment model (Fig. 5c) can be directly compared to geologic observations of surface slip (Fig. 6). The geologic slip measurements (Treiman *et al.*, 2002) are point estimates and show significant variability over short distances, while the model estimates are averages over $\sim 2.6\ km^2$ areas and are therefore smoother. The model estimates generally agree with the range of the geologic estimates with a few exceptions. The model predicts significantly more surface slip (2.4-m maximum) on the northeast branch (Fig. 3, BB′) than was observed (0.1-m maximum). This result suggests that there may have been significant slip in the subsurface that did not reach the surface and is consistent with previous geodetic inversions. There is a lack of geodetic data near the surface trace of the northeast branch (Fig. 4) and near-surface slip in the model is therefore poorly constrained. The model also predicts more slip on the Lavic Lake fault (Fig. 3, northern end of AA′) just north of its intersection with the northeast branch than was observed geologically. This area is in the transition from the Bullion Mountains to younger alluvial fan deposits and may therefore have been an area where surface rupture was distributed or otherwise difficult to fully quantify. The slip on the small linking structure (DD′) is also overestimated but is poorly constrained by near-field geodetic data. The last area of significant difference is at the southern end of the West Bullion fault (Fig. 3, southern end of AA′) where the geodetic model again predicts more slip than was observed at the surface. Previous researchers (e.g., see Simons *et al.*, 2002) also noted this discrepancy, and although additional surface rupture was identified (Treiman *et al.*, 2002), there is still a notable deficit compared to the geodetic model results. The observed surface rupture in this region was comprised of echelon cracks in alluvial fan surfaces that may have been indicative of greater right-lateral slip at depth. The comparison between the geodetic model results and geologic slip estimates suggest that the geologic estimates are generally representative of near-surface fault slip but may have a tendency to underestimate total slip due to near-surface effects such as distributed deformation in materials that may be softer and able to accommodate deformation without macroscopic fracturing.

Discussion and Conclusions

Inversion for coseismic slip using angular elastic dislocations allows for incorporation of more realistic geometries, and thus more realistic models of the seismic source. This approach takes advantage of the increasing quantity and quality of geodetic data, in particular the spatially dense near-field data acquired through interferometric radar techniques (InSAR). The flexibility of the method permits the construction of fault models with curved three-dimensional surfaces and tiplines. Fault surface traces can be taken into account, as well as subsurface constraints such as high-precision hypocentral locations of aftershocks.

The method presented here may be modified to account for the reduced resolving power with depth of geodetic data (Bos and Spakman, 2003) by adopting an adaptive meshing algorithm (e.g., Price and Bürgmann, 2002). The method may also be extended to incorporate inversion for fault geometry as well as slip. This problem is highly non linear and will require damping of the fault geometric roughness as well as slip roughness to obtain physically reasonable solutions.

In the case of the Hector Mine earthquake we have demonstrated that the method not only provides grossly similar results to previous approaches using rectangular dislocations, but also improves upon these results by removing artifacts associated with overlaps between rectangular fault segments. By constructing a model that honors the geometry of observed surface ruptures we have demonstrated that the fault geometry suggested by these data can be incorporated into the model and also leads to an improvement in the quality of the solution.

Acknowledgments

We are particularly grateful to S. Jónsson, P. Segall, and H. Zebker for sharing InSAR data from the Hector Mine earthquake and modeling experience, both of which were invaluable in our development and evaluation of P3Dinv. Thanks to D. Agnew for providing campaign GPS data and K. Kendrick for providing surface slip data for the Hector Mine earthquake. J. Muller helped with the modification of the FNNLS solver to allow for variable constraints. Thanks to two anonymous reviewers whose suggestions significantly improved this manuscript. Funding for this research was provided in part by the USGS National Earthquake Hazard Reduction Program external grant 02HQGR0050, the ARCO Stanford Graduate Fellowship to P. Resor, and the Stanford Rock Fracture Project.

References

Agnew, D., S. Owen, Z. Shen, G. Anderson, J. Svarc, H. Johnson, K. Austin, and R. Reilinger (2002). Coseismic displacements from the Hector Mine, California, earthquake: results from survey-mode global positioning system measurements, *Bull. Seism. Soc. Am.* **92,** 1355–1364.

Aydin, A., and D. Kalafat (2002). Surface ruptures of the 17 August and 12 November 1999 Izmit and Duzce earthquakes in northwestern Anatolia, Turkey: their tectonic and kinematic significance and the associated damage, *Bull. Seism. Soc. Am.* **92,** 95–106.

Bos, A. G., and W. Spakman (2003). The resolving power of coseismic surface displacement data for fault slip distribution at depth, *Geophys. Res. Lett.* **30,** 2110, doi 10.1029/2003GL017946.

Bro, R., and S. de Jong (1997). A fast non-negativity-constrained least squares algorithm, *J. Chemom.* **11,** 393–401.

Bürgmann, R., M. Ayhan, E. Fielding, T. Wright, S. McClusky, B. Aktug, C. Demir, O. Lenk, and A. Turkezer (2002). Deformation during the 12 November 1999 Duzce, Turkey, earthquake, from GPS and InSAR data, *Bull. Seism. Soc. Am.* **92,** 161–171.

Carena, S., and J. Suppe (2002). Three-dimensional imaging of active structures using earthquake aftershocks: the Northridge thrust, California, *J. Struct. Geol.* **24,** 887–904.

Cartwright, J. A., B. D. Trudgill, and C. S. Mansfield (1995). Fault growth

by segment linkage: an explanation for scatter in maximum displacement and trace length data from the Canyonlands Grabens of SE Utah, *J. Struct. Geol.* **17,** 1319–1326.

Centroid Moment Tensor (CMT) Catalog, www.seismology.harvard.edu/CMTsearch.html (last accessed August 2003).

Cervelli, P., M. Murray, P. Segall, Y. Aoki, and T. Kato (2001). Estimating source parameters from deformation data, with an application to the March 1997 earthquake swarm off the Izu Peninsula, Japan, *J. Geophys. Res.* **106,** 11,217–11,237.

Chiaraluce, L., W. Ellsworth, C. Chiarabba, and M. Cocco (2003). Imaging the complexity of an active normal fault system: the 1997 Colfiorito (central Italy) case study, *J. Geophys. Res.* **108,** 2294.

Comninou, M., and J. Dundurs (1975). Angular dilocation in a half space, *J. Elasticity* **5,** 203–216.

Desbrun, M., M. Meyer, P. Schroder, and A. H. Barr (1999). Implicit fairing of irregular meshes using diffusion and curvature flow, *SIGGRAPH* **99,** 317–324.

Du, Y., A. Aydin, and P. Segall (1992). Comparison of various inversion techniques as applied to the determination of a geophysical deformation model for the 1983 Borah Peak earthquake, *Bull. Seism. Soc. Am.* **82,** 1840–1866.

Dziewonski, A., G. Ekstrom, and N. Maternovskaya (2000). Centroid-moment tensor solutions for October-December, 1999, *Phys. Earth Planet. Inter.* **121,** 205–221.

Feigl, K., A. Sergent , and D. Jacq (1995). Estimation of an earthquake focal mechanism from a satellite radar interferogram—application to the December 4, 1992 Landers aftershock, *Geophys. Res. Lett.* **22,** 1037–1040.

Fialko, Y., M. Simons, and D. Agnew (2001). The complete (3-D) surface displacement field in the epicentral area of the 1999 M(w) 7.1 Hector Mine earthquake, California, from space geodetic observations, *Geophys. Res. Lett.* **28,** 3063–3066.

Freymueller, J., N. King, and P. Segall (1994). The coseismic slip distribution of the Landers earthquake, *Bull. Seism. Soc. Am.* **84,** 646–659.

Hanssen, R. F. (2001). *Radar interferometry: data interpretation and error analysis, in Remote Sensing and Digital Image Processing*, Kluwer Academic Publishers, Dordrecht, The Netherlands, 328 pp.

Harris, R. A., and P. Segall (1987). Detection of a locked zone at depth on the Parkfield, California, segment of the San Andreas fault, *J. Geophys. Res.* **92,** 7945–7962.

Hauksson, E., L. Jones, and K. Hutton (2002). The 1999 M_w 7.1 Hector Mine, California, earthquake sequence: complex conjugate strike-slip faulting, *Bull. Seism. Soc. Am.* **92,** 1154–1170.

Hurst, K., D. Argus, A. Donnellan, M. Heflin, D. Jefferson, G. Lyzenga, J. Parker, M. Smith, F. Webb, and J. Zumberge (2000). The coseismic geodetic signature of the 1999 Hector Mine Earthquake, *Geophys. Res. Lett.* **27,** 2733–2736.

Jeyakumaran, M., J. W. Rudnicki, and L. M. Keer (1992). Modeling slip zones with triangular dislocation elements, *Bull. Seism. Soc. Am.* **82,** 2153–2169.

Ji, C., D. Wald, and D. Helmberger (2002). Source description of the 1999 Hector Mine, California, earthquake, part II: complexity of slip history, *Bull. Seism. Soc. Am.* **92,** 1208–1226.

Johnson, K., Y. Hsu, P. Segall, and S. Yu (2001). Fault geometry and slip distribution of the 1999 Chi-Chi, Taiwan, earthquake imaged from inversion of GPS data, *Geophys. Res. Lett.* **28,** 2285–2288.

Jónsson, S., H. Zebker, P. Segall, and F. Amelung (2002). Fault slip distribution of the 1999 M_w 7.1 Hector Mine, California, earthquake, estimated from satellite radar and GPS measurements, *Bull. Seism. Soc. Am.* **92,** 1377–1389.

Jost, M. L., and R. B. Herrman (1989). A student's guide to and review of moment tensors, *Seism. Res. Lett.* **60,** 37–57.

Kattenhorn, S. A., and D. D. Pollard (2001). Integrating 3-D seismic data, field analogs, and mechanical models in the analysis of segmented normal faults in the Wytch Farm oil field, southern England, United Kingdom, *AAPG Bull.* **85,** 1183–1210.

Kaverina, A., D. Dreger, and E. Price (2002). The combined inversion of seismic and geodetic data for the source process of the 16 October 1999 M_w 7.1 Hector Mine, California, earthquake, *Bull. Seism. Soc. Am.* **92,** 1266–1280.

Kilb, D., and A. Rubin (2002). Implications of diverse fault orientations imaged in relocated aftershocks of the Mount Lewis, M_L 5.7, California, earthquake *J. Geophys. Res.* **107,** 2294.

Lin, A., T. Ouchi, A. Chen, and T. Maruyama (2001). Co-seismic displacements, folding and shortening structures along the Chelungpu surface rupture zone occurred during the 1999 Chi-Chi (Taiwan) earthquake, *Tectonophysics* **330,** 225–244.

Lin, J., and R. S. Stein (1989). Coseismic folding, earthquake recurrence, and the 1987 source mechanism at Whittier Narrows, Los Angeles Basin, California, *J. Geophys. Res.* **94,** 9614–9632.

Maerten, L., D. D. Pollard, and R. Karpuz (2000). How to constrain 3D fault continuity and linkage using reflection seismic data: a geomechanical approach, *AAPG Bull.* **84,** 1311–1324.

Martel, S. J. (1990). Formation of compound strike-slip fault zones, Mount Abbot quadrangle, California, *J. Struct. Geol.* **12,** 869–882.

Menke, W. (1984). *Geophysical Data Analysis: Discrete Inverse Theory*, International Geophysics Series, Academic, San Diego, 260 pp.

Okada, Y. (1985). Surface deformation due to shear and tensile faults in a half-space, *Bull. Seism. Soc. Am.* **75,** 1135–1154.

Peacock, D. (2002). Propagation, interaction and linkage in normal fault systems, *Earth Sci. Rev.* **58,** 121–142.

Price, E., and R. Bürgmann (2002). Interactions between the Landers and Hector Mine, California, earthquakes from space geodesy, boundary element modeling, and time-dependent friction, *Bull. Seism. Soc. Am.* **92,** 1450–1469.

Reilinger, R., S. Ergintav, R. Bürgmann, S. McClusky, O. Lenk, A. Barka, O. Gurkan, L. Hearn, K. Feigl, R. Cakmak, B. Aktug, H. Ozener, and M. Toksoz (2000). Coseismic and postseismic fault slip for the 17 August 1999, M = 7.5, Izmit, Turkey earthquake, *Science* **289,** 1519–1524.

Sandwell, D., L. Sichoix, and B. Smith (2002). The 1999 Hector Mine earthquake, southern California: vector near-field displacements from ERS InSAR, *Bull. Seism. Soc. Am.* **92,** 1341–1354.

Simons, M., Y. Fialko, and L. Rivera (2002). Coseismic deformation from the 1999 M_w 7.1 Hector Mine, California, earthquake as inferred from InSAR and GPS observations, *Bull. Seism. Soc. Am.* **92,** 1390–1402.

Stein, R. S., and S. E. Barrientos (1985). Planar high-angle faulting in the Basin and Range: geodetic analysis of the 1983 Borah Peak, Idaho, earthquake, *J. Geophys. Res.* **90,** 11,355–11,366.

Thomas, A. L. (1993). Poly3D: a three-dimensional, polygonal element, displacement discontinuity boundary element computer program with applications to fractures, faults, and cavaties in the earth's crust, *M.S. Thesis*, Stanford University, 221 pp.

Treiman, J., K. Kendrick, W. Bryant, T. Rockwell, and S. McGill (2002). Primary surface rupture associated with the M_w 7.1 16 October 1999 Hector Mine earthquake, San Bernardino County, California, *Bull. Seism. Soc. Am.* **92,** 1171–1191.

Waldhauser, F., and W. L. Ellsworth (2000). A double-difference earthquake location algorithm: method and application to the northern Hayward fault, California, *Bull. Seism. Soc. Am.* **90,** 1353–1368.

Walsh, J. J., J. Watterson, W. R. Bailey, and C. Childs (1999). Fault relays, bends and branch-lines, *J. Struct. Geol.* **21,** 1019–1026.

Willemse, E. J. M., D. C. P. Peacock, and A. Aydin (1997). Nucleation and growth of strike-slip faults in limestones from Somerset, U.K., *J. Struct. Geol.* **19,** 1461–1477.

Willemse, E. J. M., D. D. Pollard, and A. Aydin (1996). Three-dimensional analyses of slip distributions on normal fault arrays with consequences for fault scaling, *J. Struct. Geol.* **18,** 295–309.

Wright, T., B. Parsons, J. Jackson, M. Haynes, E. Fielding, P. England, and P. Clarke (1999). Source parameters of the 1 October 1995 Dinar (Turkey) earthquake from SAR interferometry and seismic bodywave modelling, *Earth Planet. Sci. Lett.* **172,** 23–37.

Yoffe, E. (1960). The angular dislocation, *Philosophical Magazine* **5,** 161–175.

Yu, E., and P. Segall (1996). Slip in the 1868 Hayward earthquake from the analysis of historical triangulation data, *J. Geophys. Res.* **101,** 16,101–16,118.

Zhang, P., F. Mao, and D. Slemmons (1999). Rupture terminations and size of segment boundaries from historical earthquake ruptures in the Basin and Range Province, *Tectonophysics* **308,** 37–52.

Department of Geological and Environmental Sciences
Stanford University
Stanford, California 94305-2115
presor@wesleyan.edu

Manuscript received 29 August 2003.